ARTICLE IN PRESS

Chemical Engineering Journal xxx (xxxx) xxx

Contents lists available at ScienceDirect

Chemical Engineering Journal

journal homepage: www.elsevier.com/locate/cej

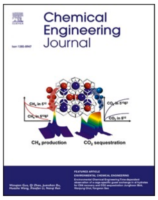

Facile ball-milling synthesis of CeO_2/g-C_3N_4 Z-scheme heterojunction for synergistic adsorption and photodegradation of methylene blue: Characteristics, kinetics, models, and mechanisms

Xiaoqian Wei [a,b], Xin Wang [a], Yu Pu [a], Annai Liu [a], Chong Chen [a], Weixin Zou [a,*], Yulin Zheng [b], Jinsheng Huang [b], Yue Zhang [b], Yicheng Yang [b], Mu. Naushad [c,d], Bin Gao [b], Lin Dong [a,*]

[a] *Key Laboratory of Mesoscopic Chemistry of MOE, School of Chemistry and Chemical Engineering, Jiangsu Key Laboratory of Vehicle Emissions Control, School of the Environmental, Center of Modern Analysis, Nanjing University, Nanjing 210093, PR China*

[b] *Department of Agricultural and Biological Engineering, University of Florida, Gainesville, FL 32611, United States*

[c] *Advanced Materials Research Chair, Chemistry Department, College of Sciences, King Saud University, Riyadh 11451, Saudi Arabia*

[d] *Yonsei Frontier Lab, Yonsei University, Seoul, Korea*

ARTICLE INFO

Keywords:
Ball milling synthesis
Z-scheme heterojunction
CeO_2/g-C_3N_4
Adsorption-photocatalytic degradation
Synergistic interaction

ABSTRACT

As a green solvent-free process, ball milling has attracted considerable attention in fabricating nanocomposites. Herein, we synthesized novel Z-scheme heterojunction CeO_2/g-C_3N_4 nanocomposites by simply direct ball milling CeO_2 and g-C_3N_4 at three different mass ratios (3:7, 7:3, and 9:1). In comparison to individual CeO_2 and g-C_3N_4, the ball-milled nanocomposites showed stronger UV light response, higher charge carrier separation efficiency, greater photodegradation potential, higher photocurrent intensity, and faster electron transfer, indicating much better photocatalytic activity. When used as photocatalysts to remove methylene blue (MB) under UV light irradiation, 70% CeO_2/g-C_3N_4 exhibited the highest removal rate (90.1%), much better than that of CeO_2 (6.2%) or g-C_3N_4 (45.7%). The synergistic interact between adsorption and photodegradation of the CeO_2/g-C_3N_4 nanocomposites was simulated by kinetic models, and a strong positive correlation ($r = 0.834$ and $r_s = 0.777$) between adsorption and photocatalysis was identified. The results indicate that adsorption can promote photodegradation by accelerating the kinetics, while photodegradation can regenerate adsorption sites. This work provides not only a facile synthesis of Z-scheme heterojunction photocatalysts but also a novel perspective for better understanding the synergy between adsorption and photocatalysis.

1. Introduction

With rapid industrialization and urbanization, energy crisis and environmental pollution have become serious global issues faced by humans [1–3]. Heterogeneous photocatalysis is regarded as a promising and “green” technology to dispose environmental contaminants (especially organic dyes) [4,5]. Owing to the disadvantages of intrinsic wide bandgap, rapid electron-hole pair recombination, and low degradation efficiency, the application of most traditional photocatalysts (TiO_2 [6], ZnO [7], etc.) has been limited. As a result, it is crucial and imperative to develop highly effective photocatalysts with enhanced band structures, chemical stability, charge carrier separation and transportation, and electron-hole recombination [8–10]. Until now, a wide variety of effective strategies have been developed to tackle the aforementioned issues, for instance, doping with metallic/nonmetallic elements [11], fabricating heterojunctions [12], depositing noble metal [13], and so on. Among these methods, constructing heterojunctions has been identified as a desirable way for facilitating the photocatalytic performance. This staggered band structure can form a close interface and built a strong inner electronic field near the interface, leading to efficient transfer and separation of photogenerated charge carriers and improvement of light absorption ability [14]. Especially, a Z-scheme heterojunction with high redox potential and effective spatial charge separation exhibits the excellent photocatalytic performance, which can effectively remove contaminants [15].

Owing to their low cost, high stability, proper band structure and excellent redox ability, cerium dioxide (CeO_2) and graphic carbon nitrite (g-C_3N_4) have been widely used as photocatalysts in various

---

* Corresponding authors.
E-mail addresses: wxzou2016@nju.edu.cn (W. Zou), donglin@nju.edu.cn (L. Dong).

https://doi.org/10.1016/j.cej.2020.127719
Received 23 September 2020; Received in revised form 5 November 2020; Accepted 10 November 2020

Please cite this article as: Xiaoqian Wei, *Chemical Engineering Journal*, https://doi.org/10.1016/j.cej.2020.127719

applications such as photocatalytic CO_2 reduction, contaminant decomposing, and water splitting [8,16–21]. Recent studies have demonstrated that suitably engineered heterojunctions of CeO_2 and g-C_3N_4 (i.e., CeO_2/g-C_3N_4) possess an improved photocatalytic activity [22–25]. Ma et al. synthesized a type-II CeO_2/g-C_3N_4 nanosheet heterojunction via a solid-state thermolysis method, showing superior photocatalytic performances compared with individual g-C_3N_4 and CeO_2 [25]. Sreekanth and coworkers successfully coupled carbon-vacancy-promoted g-C_3N_4 to low defect-mediated CeO_2 through a simple in situ hydrothermal synthetic technique, and the resultant g-C_3N_4/CeO_2 heterojunction displays remarkable photodegradation efficiency to RhB in the presence of $NaBH_4$ [26]. A microwave-mediated solvothermal route has been developed to synthesize CeO_2/g-C_3N_4 heterojunctions with improved oxygen reduction reaction activity and electrochemical stability [27].

Ball milling, a facile, effective, and eco-friendly (solvent-free or minimal solvent) technique, has been recently applied as a green and cost-effective method to fabricate composited photocatalysts [28–30]. It has been revealed that ball milling can introduce defects and new active edge sites to enhance the stability and activity of the composited catalysts [31]. Zhu et al. highlighted that ball milling can promote dispersion of SnO_2 nanoparticles to strengthen the bonding between SnO_2 and g-C_3N_4 [32]. Wang et al. demonstrated that surface area and band gap energy of g-C_3N_4-based photocatalysts can be enlarged by ball milling [33]. Guo and collaborators successfully prepared the heterojunction g-C_3N_4/$Bi_4Ti_3O_{12}$ photocatalyst by a facile ball milling way and the catalyst possessed an enhanced photocatalytic behavior for the removal of AO-7 [34]. Therefore, the ball milling technology possesses potential application in the synthesis of heterojunction photocatalysts. To the best of our knowledge, however, none of the previous studies has explored the ball milling synthesis of CeO_2/g-C_3N_4 photocatalyst, and the kinetic relationship between the adsorptive and photocatalytic contaminant removal on CeO_2/g-C_3N_4 has not been evaluated yet.

To fill these knowledge gaps, we prepared heterojunction CeO_2/g-C_3N_4 photocatalysts for the first time through a solvent-free ball milling strategy, simultaneously, the adsorptive and photocatalytic performances were determined on the model contaminant MB, in which the removal process under light illumination were assessed through kinetic models. The objectives of this work are as follows: (1) optimize the ball milling synthesis of CeO_2/g-C_3N_4 photocatalysts; (2) characterize their physicochemical and photoelectric properties; (3) determine the built-in electric field on CeO_2/g-C_3N_4 interfaces; (4) measure and model the adsorption and photocatalytic degradation kinetics of MB by CeO_2/g-C_3N_4; and (5) unveil the governing mechanisms of the synergy between adsorption and photodegradation.

2. Experimental section

2.1. Catalyst preparation

Deionized (DI) water was used for all experiments. All the chemicals are at least analytical grade and were used as received without further purification.

The g-C_3N_4 powder was obtained through calcination of urea precursor. Briefly, 10 g of urea was put into an alumina crucible with a cover, which can form a semi-closed system to prevent sublimation. Afterward, it was heated to 520 °C for 2 h with a heating rate of 5 °C min^{-1} in a muffle furnace. Then cooling to room temperature, the yellow powder (g-C_3N_4) was ground and collected.

The heterojunction photocatalyst CeO_2/g-C_3N_4 composites were prepared via a simple ball milling method. The typical synthesis procedure was as follows: CeO_2 and g-C_3N_4 mixtures of different mass ratios (1.8 g in total) were placed in a planetary ball mill machine (PQ-N2, USA) within 500 mL agate jars, and 180 g balls were subsequently added into each jar. The ball milling operation was carried out at a rotational speed of 500 rpm for 12 h in ambient air. The obtained samples are denoted as x% CeO_2/g-C_3N_4, where x% represents the mass ratio of CeO_2 in the composites. For comparison, CeO_2 or g-C_3N_4 was also ball milled under the same conditions and is still denoted as CeO_2 or g-C_3N_4.

2.2. Catalyst characterization

The descriptions of the characterization details are reported in the supporting information (S1).

2.3. Evaluation of adsorption and photocatalytic performance

The batch adsorption and photodegradation of MB were carried out under the irradiation of a 36 W UV lamp (OS72) with the wavelength of 254 nm. 0.05 g of the prepared samples powder (dosage of 0.5 g L^{-1}) were dispersed into 100 mL of 10 mg L^{-1} MB solutions in 250 mL quartz vessels. The suspensions were mechanically stirred maintaining at 25 °C. For each sample, MB removal was tested under two conditions, one in a dark chamber and the other under UV light illumination. During the experiment, 4 mL of the solution were periodically withdrawn (i.e., 30, 60, 90, 120, 150, and 180 min) from the vessels. The samples were filtered through 0.22 μm pore size nylon membrane filters (MCE Syringe Filter, China) and MB concentrations in the filtrates were determined using a UV–Vis spectrophotometer (EVO 60, Thermo Scientific, USA) at wavelength of 664 nm. The reusability of the photocatalyst was evaluated with four consecutive 3-h recycles of MB photodegradation. After each cycle, the used catalyst was collected through centrifugation, washed with ethanol and DI water for several times, and oven dried for next use.

2.4. Kinetic models

Several models have been developed to describe the adsorption and photodegradation kinetic data [35,36]. For the convenience of comparison, the commonly used first-order kinetic model and the modified Elovich model were applied to simulate the experimental data. While the first order kinetic model describes homogeneous removal of the target compound at a constant rate; the modified Elovich model is a heterogeneous model controlled by multiple processes [36]. The governing equations of the two models are as follows:

$$\frac{dC_t}{dt} = -kC_t \quad \text{first} - \text{order model} \tag{1}$$

$$\frac{dC_t}{dt} = -KC_0 exp(\beta(C_t - C_0)) \quad \text{modified Elovich model} \tag{2}$$

where C_0 and Ct are the concentrations (mg L^{-1}) of MB at time 0 and at any time t, respectively; k (min^{-1}) and K (min^{-1}) represent the removal rate constant for the first-Order model and the modified Elovich model, respectively; and β is a constant inversely proportional to removal capacity.

3. Results and discussion

3.1. Morphology, structural and chemical composition

The surface morphology and microstructure of the as-synthesized CeO_2, g-C_3N_4 and 70% CeO_2/g-C_3N_4 photocatalysts were examined with SEM. The milled CeO_2 powders exhibited irregular nano-sized particles and partial severely agglomerated structure (Fig. S1a, supporting information), confirming the formation of ultrafine nanoparticles. Due to the high energy ball milling process, the large bulk g-C_3N_4 powder was exfoliated into aggregation of small fragments (Fig. S1b). Similar morphology was found in the 70% CeO_2/g-C_3N_4 sample, in which irregular shaped CeO_2 particles of 2–70 nm were dispersed on the surface of the g-C_3N_4 fragments (Fig. 1a). The surface of the composite was rough and porous (Fig. 1b), which is beneficial to its

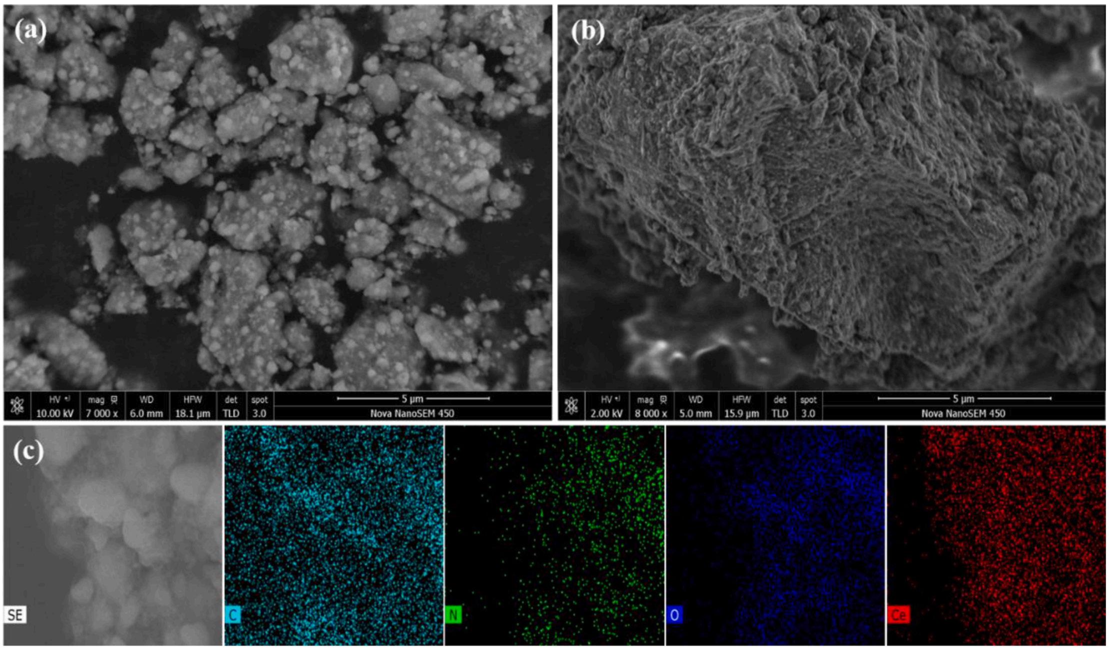

Fig. 1. SEM images (a and b) and the corresponding energy-dispersive X-ray spectroscopy (EDX) elemental mapping (c) of 70% CeO_2/g-C_3N_4 composite.

adsorptive and photocatalytic ability. EDX elemental mapping of the 70% CeO_2/g-C_3N_4 sample (Fig. 1c) was performed to explore its surface element composition. C, N, O, and Ce elements were found to be uniformly distributed on the surface of the composite, confirming that ball milling infused CeO_2 and g-C_3N_4. These results clearly demonstrate the success of ball milling method in synthesis of the CeO_2/g-C_3N_4 composites.

TEM and HRTEM were employed to further examine morphologic details and the interface between CeO_2 and g-C_3N_4 in the 70% CeO_2/g-C_3N_4 composite. The ball-milled CeO_2 particles showed agglomerated morphology (Fig. S2a); while the g-C_3N_4 was milled into a thin lamellar-like structure and the darker part of the image can be attributed to overlap of g-C_3N_4 sheets (Fig. S2b). In the 70% CeO_2/g-C_3N_4 composite, ultrafine CeO_2 nanocrystals were found to be anchored irregularly onto the surface of g-C_3N_4 (Fig. S2c). Although the CeO_2 particles had agglomerated to some extent, they were in direct contact with the g-C_3N_4 surface, which can provide additional photocatalytic reaction sites. The joint between CeO_2 and g-C_3N_4 showed a clear interface (Fig. S2d), evidencing the formation of a well-defined heterojunction of CeO_2/g-C_3N_4 [37]. Moreover, the CeO_2 possessed a well-crystallized phase and the lattice fringes with spacing of 0.27 nm (Fig. S2d), corresponding to the exposed (200) crystal plane of CeO_2 (JCPDS card No. 34–0394) [25]. Such close interfacial contact and perfect crystalline quality are favorable for the efficient separation and transfer of photogenerated charge carriers, which can greatly improve the photocatalytic performance of the CeO_2/g-C_3N_4 composite.

To identify composition and phase structure of the synthesized materials, the XPS spectra were determined (Fig. S3). The high-resolution spectra of C 1 s and N 1 s for g-C_3N_4 and 70% CeO_2/g-C_3N_4 composite show that the structure of g-C_3N_4 has not been destroyed, and the signals of the tertiary nitrogen (N-$(C)_3$ or H-N-$(C)_2$) groups and the triazine rings (N-C = N, C = N-C) in the aromatic rings of g-C_3N_4 are present on the CeO_2/g-C_3N_4 heterostructure [38–40]. XRD analysis was carried out (Fig. S4a). In the pure g-C_3N_4, one significant diffraction peak was observed at 27.7°, which can be ascribed to the (002) plane and corresponds to the interlayer stacking interaction of aromatic systems [41]. However, the diffraction peak indexed to (100) plane was not observed, probably due to the destruction of interlayer structure during ball milling [42]. The diffraction patterns of CeO_2 and CeO_2/g-C_3N_4 composites perfectly matched the standard peaks of cubic fluorite CeO_2 (JCPDF No. 34–0394) [43]. With the increase of the g-C_3N_4 content in the CeO_2/g-C_3N_4 composites, the intensity of these peaks enhanced gradually, manifesting that g-C_3N_4 could protect CeO_2 to maintain its crystal form during ball milling. In addition, the CeO_2/g-C_3N_4 composites had slight high-angle shifts of the peak at 28.6° (Fig. S4a (right)), probably due to the interaction between CeO_2 and g-C_3N_4 [23].

The interfacial electronic interaction of the CeO_2/g-C_3N_4 composite was confirmed by FT-IR (Fig. S4b). A broad band located at 3600–3000 cm^{-1} are attributed to the physically absorbed hydroxyl (–OH) and amino (–NH_2) groups, the peaks in the 1600–1200 cm^{-1} region are the characteristic vibration modes of C = N and aromatic C–N heterocycles, and the sharp band near 804 cm^{-1} can be assigned to the typical out of plane breathing mode of the s-triazine units of g-C_3N_4 [27,44]. It is found that after the high-energy ball milling, the main structure of g-C_3N_4 was intact on the CeO_2/g-C_3N_4 composites. Interestingly, it was observed that the broad peaks ranging from 3600 to 3000 cm^{-1} became weaker, broader and slightly red-shifted on the CeO_2/g-C_3N_4 composites, due to the formed hydrogen bonds between CeO_2 and g-C_3N_4, i.e., the hydroxyl groups adsorbed on the surface of CeO_2 were hybridized with the amino groups on g-C_3N_4 [45,46].

Furthermore, the compared XPS spectra of 70% CeO_2/g-C_3N_4 and CeO_2 were employed to explore the interfacial electronic effect. In the Ce 3d peaks (Fig. 2a), the peaks of u‴ (916.5 eV), u″ (907.3 eV), u (900.7 eV), *v*‴ (898.1 eV), *v*″ (888.4 eV) and *v* (882.2 eV) are indexed to Ce^{4+}, and the other two peaks occurring at 903.2 eV (marked u′) and 884.8 eV (marked *v*′) can be ascribed to Ce^{3+} species [25]. In comparison with those of pure CeO_2, the peaks related to Ce^{4+} of the 70% CeO_2/g-C_3N_4 composite shifted toward the lower binding energy, indicating that the increased electron density on Ce of CeO_2/g-C_3N_4 led to CeO_2 with negative and g-C_3N_4 positive charges, respectively. However, the peak labeled u′ of the 70% CeO_2/g-C_3N_4 composite shifted toward the higher binding energy, which was due to the existence of the redox pairs of Ce^{4+}/Ce^{3+}. In addition, the interface electrons transfer of CeO_2/g-C_3N_4 was investigate by UPS. As shown in Fig. S5, the work function of CeO_2 and g-C_3N_4 are 4.01 eV and 3.79 eV, respectively. It demonstrates that the free electrons tend to move from g-C_3N_4 with a smaller work function to CeO_2, in order to equilibrate their fermi levels as they are in contact [47,48]. These reveal that the staggered band alignment of CeO_2

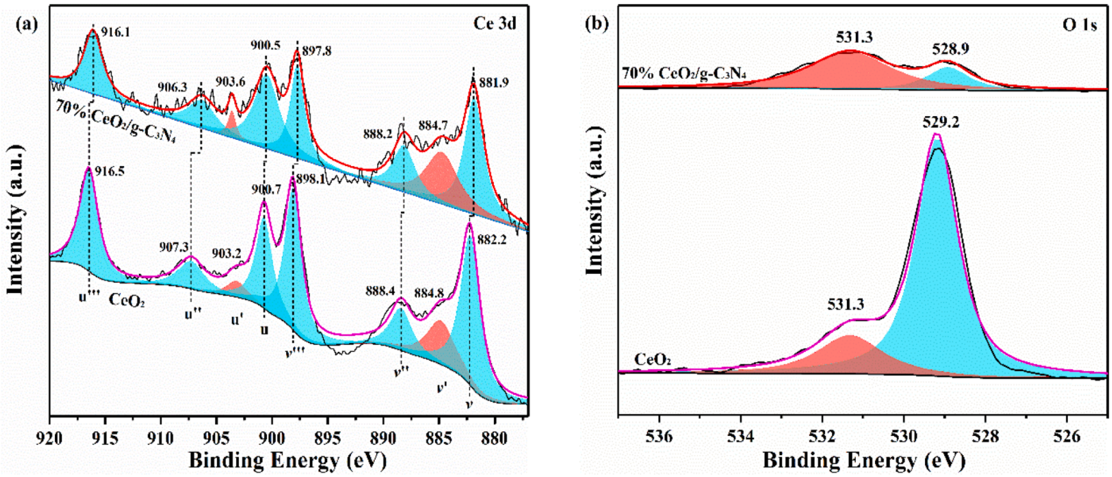

Fig. 2. XPS spectra of (a) Ce 3d, and (b) O 1 s of 70% CeO_2/g-C_3N_4 and CeO_2.

and g-C_3N_4 result in the formation of internal electric filed on CeO_2/g-C_3N_4 heterojunction. Moreover, the XPS spectra of O 1 s were showed in Fig. 2b. The peak observed at 529.2 eV can associated with the lattice oxygen O^{2-} (in the Ce–O bond of CeO_2), along with the weak shoulder peak near 531.3 eV can be related to the chemisorbed oxygen on the surface of the catalysts (–OH group and oxygen-containing species) [49]. It was found that more chemisorbed oxygen species formed on 70% CeO_2/g-C_3N_4 surface (75.8%) compared with CeO_2 (20.0%). According to the order of Ce^{3+}/ (Ce^{3+} + Ce^{4+}) ratios, i.e., 70% CeO_2/g-C_3N_4 (18.4%) > CeO_2 (12.8%), it is proposed that more oxygen defect formation onto 70% CeO_2/g-C_3N_4 ($Ce^{4+}+O_L \rightarrow Ce^{3+}+O_V$), and thus is beneficial for more surface oxygen species generation [46].

On the basis of XRD, FT-IR, XPS and UPS results, it was suggested that the ball milling method made the interface electrons transfer from g-C_3N_4 to CeO_2, leading to the formation of built-in electric field, more oxygen defect, and surface adsorption oxygen species on CeO_2/g-C_3N_4 heterojunction.

3.2. Band structures and charge transfer

The optical and photoelectric properties of photocatalysts are critical to their photocatalytic performance. The UV–vis diffuse reflectance spectroscopy (DRS) was utilized to examine the optical absorption properties and band gaps of CeO_2, g-C_3N_4, and CeO_2/g-C_3N_4 composites (Fig. 3a, S6a). Owing to its intrinsic band structure, CeO_2 displayed the highest optical absorption in the ultraviolet light region with the band edge at around 468 nm. While the as-synthesized CeO_2/g-C_3N_4 composites showed a distinct blue shift with respect to CeO_2, which might be resulted from the famous quantum confinement effect originated from refinement of the materials by ball milling process [50]. Among these composites, 70% CeO_2/g-C_3N_4 composite showed the strongest light response. According to the Kubelka-Munk function, the plot of $(Ah\nu)^{2/n}$ versus $h\nu$ in Fig. 3a determined the band gap energies (Eg) of CeO_2 and g-C_3N_4 catalysts. The estimated Eg values were approximately 2.81 and 2.76 eV corresponding to CeO_2 ($n = 1$) and g-C_3N_4 ($n = 4$), respectively.

Furthermore, the valence band (VB) XPS and Mott–Schottky (M−S) tests were introduced to determine the VB and conduction band (CB) position of CeO_2 and g-C_3N_4, respectively. Fig. 3b depicts the VB XPS spectra of CeO_2 and g-C_3N_4. The value of CeO_2 occurred at about 2.03 eV, higher than that of g-C_3N_4 (1.75 eV). In addition, both CeO_2 (Fig. 3c) and g-C_3N_4 (Fig. 3d) showed the positive tangent slopes of M−S plots (C^{-2} vs. V) corresponding to n-type semiconductor property with electrons as the main carriers [51]. The calculated values of the flat band potentials for CeO_2 and g-C_3N_4 were reckoned up to be −1.21 and −1.44 V (vs. Ag/AgCl), which are equivalent to −0.58 and −0.81 V (vs. NHE), respectively [52]. The meaning of flat band potential is that the Fermi level position relative to the electrochemical potential of redox couple in the electrolyte. The Fermi level of g-C_3N_4 is higher than that of CeO_2, suggesting that the electrons are easily transferred from g-C_3N_4 to CeO_2 to equilibrate their fermi levels, which is consistent with the results of XPS and UPS [47,53]. The widely accepted fact is that the CB potentials with respect to n-type semiconductors are usually 0.1–0.3 eV more negative than the flat band potentials [24]. Therefore, the E_{CB} of CeO_2 in this work was about −0.78 eV (vs. NHE). Whereas for g-C_3N_4, the CB lay at −1.01 eV (vs. NHE). The obtained CB and VB values of CeO_2 and g-C_3N_4 in this work are very similar to the previous literature reports [54]. Therefore, based on the obtained values of CB and VB and the pervasive formula: $E_g = E_{VB}–E_{CB}$, the Eg values of CeO_2 and g-C_3N_4 were 2.81 and 2.76 eV, respectively, which are in accordance the results of UV–vis DRS (Fig. 3a). Therefore, the band structures of CeO_2/g-C_3N_4 heterostructure were displayed in Fig. 3e, under the guidance of built-in electronic effect, negative and positive charges were showed on CeO_2 and g-C_3N_4, respectively, thermodynamically leading to the faster electron transfer (Fig. 3f) and stronger redox potential on the Z-scheme CeO_2/g-C_3N_4 heterostructure.

The separation, migration, and recombination processes of generated electron-hole pairs in photocatalytic materials were determined. The PL spectra of CeO_2, g-C_3N_4, and CeO_2/g-C_3N_4 composites at an excitation wavelength of 325 nm showed similar PL emission peaks (Fig. S6b). The main emission peak centered at about 450 nm can be ascribed to the band to band PL phenomenon with the energy of the excitation light closing to the band gap energy of g-C_3N_4 and CeO_2 [25,27]. Compared with CeO_2 and g-C_3N_4, the CeO_2/g-C_3N_4 heterostructures exhibited much weaker PL emission, and the 70% CeO_2/g-C_3N_4 catalyst showed the lowest PL emission intensity, indicating the suppression of the photogenerated electron-hole pairs recombination. Thus, the 70% CeO_2/g-C_3N_4 catalyst possessed the highest charge separation efficiency, greatly boosting the photocatalytic performance.

To further explore electronic structure and interfacial charge separation dynamics of the photocatalysts, transient photocurrent responses were carried out for five on–off cycles under light illumination (Fig. S7). It is well known that a higher photocurrent intensity manifests more efficient separation and fast transfer of photo-generated electrons, and more electrons are able to participate in the photocatalytic degradation reaction, leading to a better photocatalytic performance. The photocurrent response intensity of the photocatalysts followed the order of 70% CeO_2/g-C_3N_4 > 90% CeO_2/g-C_3N_4 > 30% CeO_2/g-C_3N_4 > g-C_3N_4 > CeO_2. Furthermore, electrochemical impedance spectroscopy (EIS) test was determined in dark to explore the interfacial charge transport speed at the electrode–electrolyte interface. Typically, a smaller arc radius corresponds to a less electron transfer resistance and a faster interfacial charge transfer and separation efficiency [55]. Based on the

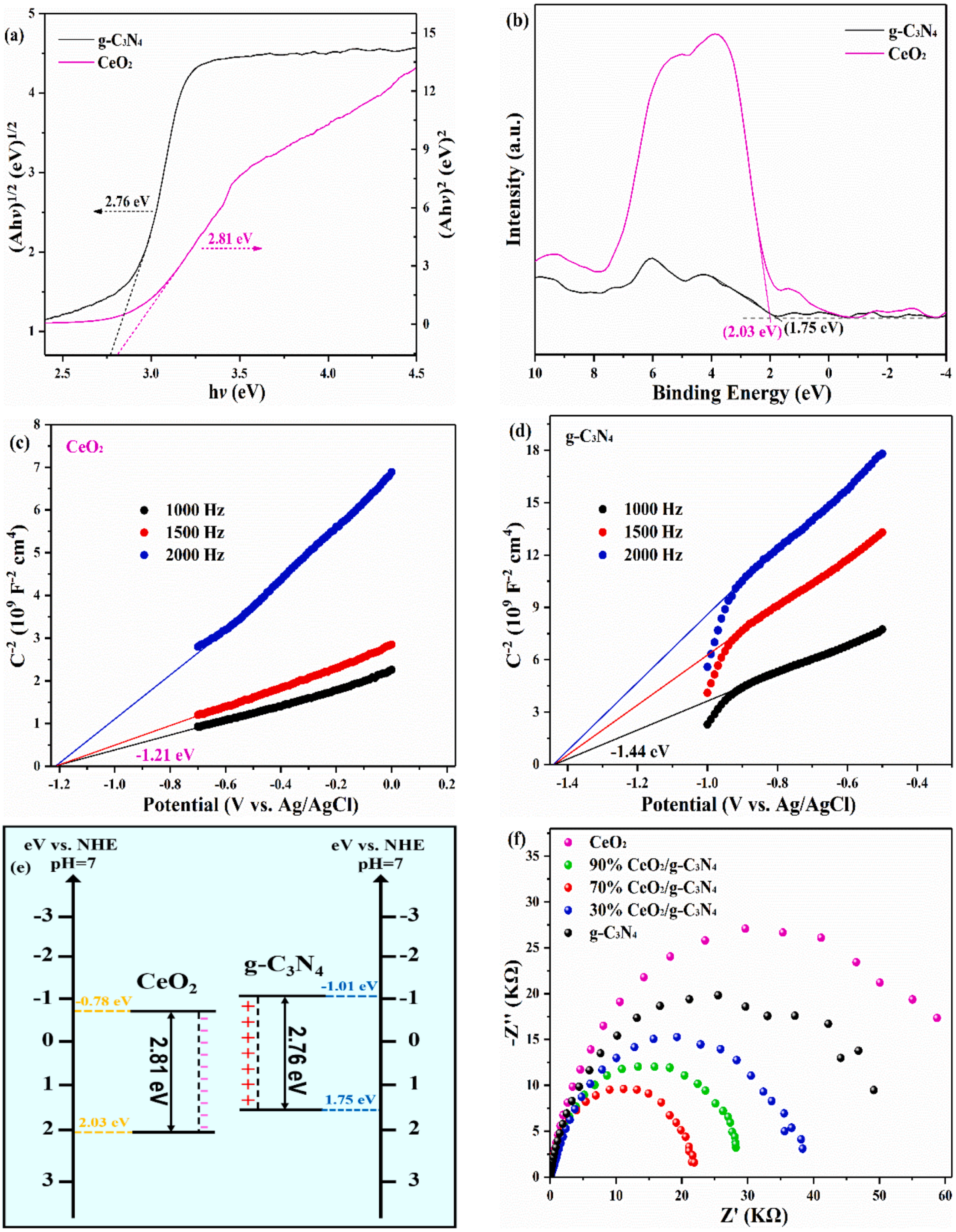

Fig. 3. Estimated band gap energies (a) and valence band XPS spectra (b) of the CeO_2 and g-C_3N_4. Mott-Schottky plots of CeO_2 (c) and g-C_3N_4 (d) at frequencies of 1000, 1500 and 2000 Hz in the 0.5 M Na_2SO_4 aqueous solution. (e) The band structures of CeO_2/g-C_3N_4 heterostructure. (f) EIS Nyquist plots of CeO_2, g-C_3N_4, and CeO_2/g-C_3N_4 composites.

observations (Fig. 3f), 70% CeO_2/g-C_3N_4 displayed the lowest charge-transfer resistance among all samples, indicating that the interfacial interaction of CeO_2/g-C_3N_4 heterojunction can greatly accelerate electron transfer and improve electron utilization thereby enhance photocatalytic performance. This is in agreement with the results of PL and transient photocurrent responses. Based on the above characterization analysis, the successfully constructed Z-scheme CeO_2/g-C_3N_4 heterostructure can significantly improve light absorption, fast interfacial electron transfer and efficient separation of photo-induced electron-hole pairs.

3.3. Kinetic model simulations for synergistic adsorption-photocatalysis

Photocatalytic degradation of MB by the photocatalysts were evaluated. A blank test without any photocatalysts was used as the control in the experiment. Only about 5.5% of MB was degraded in the blank after 180 min irradiation (Fig. 4a), indicating that self-photo degradation of MB was almost negligible. In comparison to CeO_2 and g-C_3N_4, all the

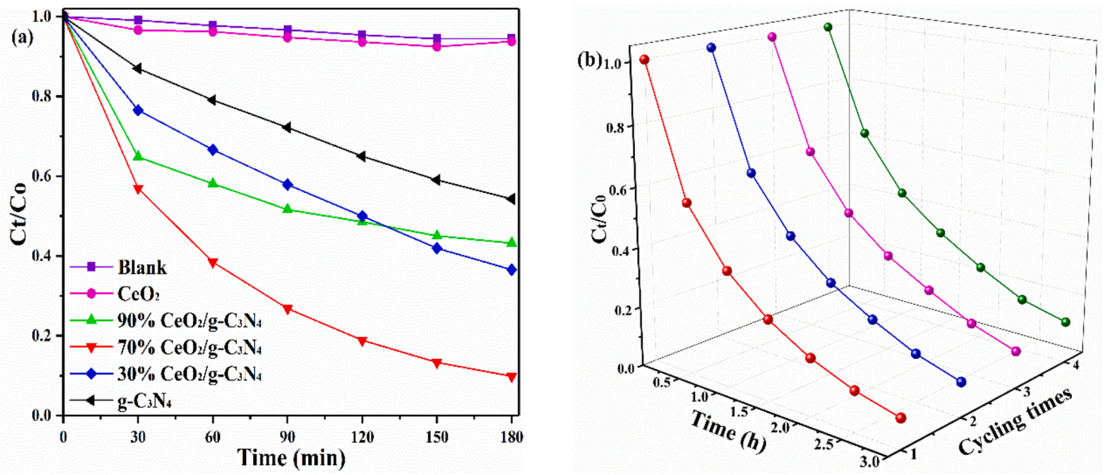

Fig. 4. Removal of MB by the photocatalysts under UV light irradiation: (a) Comparison of photocatalytic activity of the CeO_2, g-C_3N_4, and CeO_2/g-C_3N_4 composites, (b) reusability of 70% CeO_2/g-C_3N_4.

CeO_2/g-C_3N_4 composites showed much larger removal of MB during light irradiation (Fig. 4a), indicating higher activity. This can be attributed to the synergy between CeO_2 and g-C_3N_4 that can increase photogenerated charge carries separation. Among the composites, 70% CeO_2/g-C_3N_4 possessed the highest photocatalytic performance with a MB removal efficiency of 90.1% after 180 min irradiation. This is consistent with the characterization results that 70% CeO_2/g-C_3N_4 has the best photocatalytic properties in the composites. Furthermore, the performance of 70% CeO_2/g-C_3N_4 catalyst synthesized by ball milling method is better than that of conventional methods (Table S1). Comparison of the performances of the three CeO_2/g-C_3N_4 composites also reveals the importance of the ratio of CeO_2 and g-C_3N_4 to the photocatalytic activity. While the ball milling combination of CeO_2 and g-C_3N_4 activate the synergy to promote their photocatalytic activity; overdose of either of them would weaken the synergy to make the composites less effective. Because 70% CeO_2/g-C_3N_4 had the best MB removal performance, its reusability was further evaluated (Fig. 4b). The 70% CeO_2/g-C_3N_4 maintained its high MB degradation efficiency. All these results demonstrate that the heterojunction CeO_2/g-C_3N_4 is a promising photocatalyst for contaminant degradation because of its high photocatalytic activity and good reusability.

Generally, adsorption and photocatalysis are indivisible in the process of photocatalytic degradation of organic contaminants [56]. To explore the synergy between adsorption and photocatalysis, the removal kinetics of MB by the photocatalysts were measured with and without light. In the dark room (Fig. S8), the adsorption performances of the samples followed the order of 70% CeO_2/g-C_3N_4 > 90% CeO_2/g-C_3N_4 > 30% CeO_2/g-C_3N_4 > g-C_3N_4 > CeO_2. And we carried out FT-IR tests on the 70% CeO_2/g-C_3N_4 sample before and after adsorption of MB (Fig. S9). After MB adsorption, new peaks at 3000 ~ 2000 cm^{-1}, 1994 cm^{-1} and 1920 cm^{-1} assigned to C–H, -C = C = N and -C = C = C- appeared, suggesting that MB molecules adsorbed strongly on the surface of 70% CeO_2/g-C_3N_4 by π-π stacking interactions between the aromatic backbone of the MB and the highly delocalized π-conjugated system of g-C_3N_4. No obvious changes of the broad peaks between 3500 and 3000 cm^{-1}attributed oxygen-containing functional groups was observed [53,57,58]. In addition, the intensity of the peak at 804 cm^{-1} assigned to the s-triazine units of g-C_3N_4 became weaker relative to the peaks in the 1600–1200 cm^{-1} region, indicating that MB molecules interacted with π-π of the triazine ring. The order of adsorption performances of the samples in agreement with the trend of their photodegradation ability (Fig. 4a), indicating that there might be a strong correlation between adsorption and photocatalysis during MB photodegradation by the samples. Furthermore, the adsorption and photodegradation experiment data on the adsorption of MB by the composites were fitted to the widely used first-order reaction kinetic model and the modified Elovich model established by our group (Fig. 5). The fitted model parameters are presented in Table 1. The adsorption and photodegradation experimental data were better fitted by the modified Elovich model ($R^2 > 0.990$) than the first-order model ($R^2 = 0.634$–0.982). The best-fit kinetic adsorption and photodegradation rate constant of the 70% CeO_2/g-C_3N_4 (0.232 min^{-1} and 0.030 min^{-1}) were larger than that of the 90% CeO_2/g-C_3N_4 (0.120 min^{-1} and 0.029 min^{-1}) and 30% CeO_2/g-C_3N_4 (0.061 min^{-1} and 0.011 min^{-1}), and the 70% CeO_2/g-C_3N_4 exhibited the highest adsorption and photodegradation capacity ($\beta_{a,70} < \beta_{a,90} < \beta_{a,30}$ and $\beta_{p,70} < \beta_{p,30} < \beta_{p,90}$), confirming that adsorption can accelerate the photocatalytic degradation process. Thus, adsorption is one of the important parameters to control the kinetic constant of MB photodegradation, and the synergy between adsorption and photocatalytic degradation might be present.

Furthermore, for the aim to further clarify the relationship between adsorption and photocatalysis, we conducted a simple correlation analysis of MB adsorption and photodegradation rates with Pearson's product-moment correlation coefficient (r) and Spearman's rank correlation coefficient (r_s) [59]. The results showed strong correlation between adsorption and photodegradation (Fig. 6). The descriptions of these correlation coefficients are shown in the supporting information (S2 and Tables S2 and S3). The obtained Pearson's ($r = 0.834$) and Spearman's ($r_s = 0.777$) correlation coefficient values are greater than statistical critical values ($Wp = 0.380$ and $Wp_s = 0.382$), manifesting that the correlation is statistically significant.

Base on the findings of this work, the superior photodegradation activity of CeO_2/g-C_3N_4 can be mainly attributed to the heterojunction structure and the synergy between adsorption and photodegradation. A schematic illustration of the mechanism of MB degradation by a Z-scheme heterojunction between CeO_2 and g-C_3N_4 is presented in Fig. 7a. The ball milling method not only endues a strong interfacial interaction through tightly bonding between CeO_2 and g-C_3N_4, but also builds an effective interfacial electronic effect enabling g-C_3N_4 and CeO_2 with positive and negative charges, respectively. Thus, driven by the inner electric field at the CeO_2/g-C_3N_4 heterojunction interface, photogenerated electrons stay on the CB of g-C_3N_4, while holes on the VB of CeO_2, which enhance the redox ability, and thermodynamically, more active oxygen radicals are easily generated. That are, e^- on the CB of g-C_3N_4 has strong reduction ability can convert O_2 into $\cdot O_2^-$ radicals ($E^{\Theta}(O_2/\cdot O_2^-) = -0.046$ eV vs. NHE) while the h^+ on the VB of CeO_2 with strong oxidation power can be taken up by surface chemical adsorbed oxygen, i.e., OH^-, to produce •OH radicals ($E^{\Theta}(OH^-/\cdot OH) = 1.99$ eV, vs. NHE) [25]. Then the generated active radical species can efficiently oxidize MB adsorbed on the surface of CeO_2/g-C_3N_4 to regenerate the

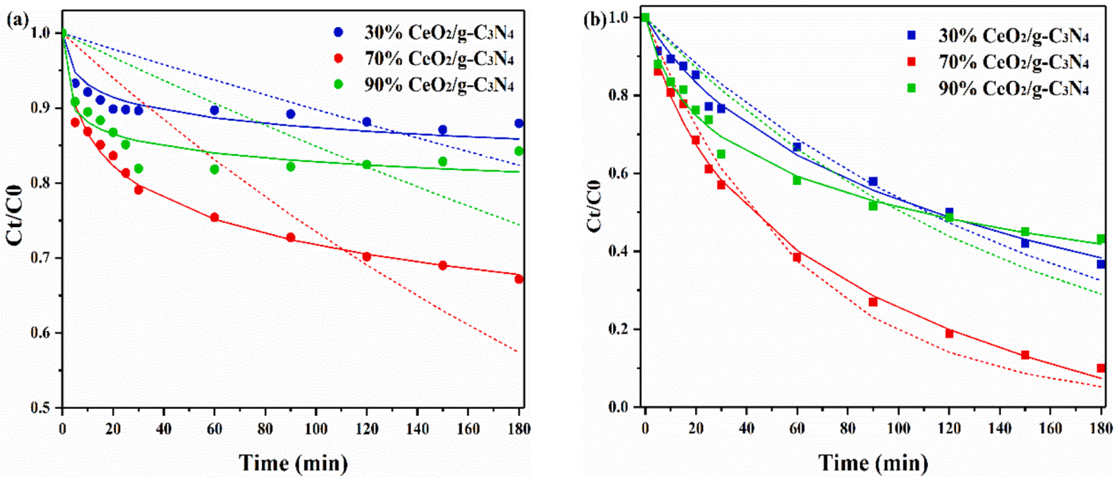

Fig. 5. Model simulations of MB removal kinetics by CeO_2/g-C_3N_4 composites in dark (a) and under UV light irradiation (b). Symbols represent experimental data. Short dash and solid lines are simulations of the first order and the modified-Elovich models.

Table 1
The fitted parameters of the kinetics models for removal of MB in dark (a) and under UV light irradiation (b).

Models	Samples	Parameter 1	Parameter 2	R^2
1st order	30% CeO_2/ g-C_3N_4	$k_{a,30} = 0.006$	–	0.700
		$k_{b,30} = 0.005$	–	0.963
	70% CeO_2/ g-C_3N_4	$k_{a,70} = 0.011$	–	0.634
		$k_{b,70} = 0.016$	–	0.982
	90% CeO_2/ g-C_3N_4	$k_{a,90} = 0.009$	–	0.664
		$k_{b,90} = 0.006$	–	0.791
Modified-Elovich	30% CeO_2/ g-C_3N_4	$K_{a,30} = 0.061$	$\beta_{a,30} = 39.640$	0.996
		$K_{b,30} = 0.011$	$\beta_{b,30} = 3.254$	0.991
	70% CeO_2/ g-C_3N_4	$K_{a,70} = 0.232$	$\beta_{a,70} = 31.261$	0.996
		$K_{b,70} = 0.030$	$\beta_{b,70} = 3.104$	0.998
	90% CeO_2/ g-C_3N_4	$K_{a,90} = 0.120$	$\beta_{a,90} = 34.529$	0.996
		$K_{b,90} = 0.029$	$\beta_{b,90} = 5.974$	0.997

adsorbed sites for capturing additional MB. This auto-recycled process can greatly improve the removal efficiency of MB by the nanocomposite [60,61]. Meanwhile, the redox pairs of Ce^{4+}/Ce^{3+} are recognized as electron and hole scavengers, inhibiting the recombination of photo-generated carriers [62]. With regard to the synergy between adsorption and photodegradation, kinetics simulation models suggest that the adsorption of contaminants (e.g., MB) on the CeO_2/g-C_3N_4 surface thus can accelerate photocatalytic degradation, meanwhile photodegradation of the adsorbed contaminants can free the adsorption sites to expand the capacity or reusability.

In addition, the Z-scheme heterojunction could generate more the active oxygen species, which are beneficial for the photodegradation of MB on the 70% CeO_2/g-C_3N_4 under light irradiation. In Fig. 7b, the trapping experiment using isopropanol (IPA), p-Benzoquinone (BQ), and Ethylenediamine tetraacetic acid (EDTA) as the scavengers of hydroxyl radical (·OH), superoxide radical ($\cdot O_2^-$), and hole (h^+), respectively, demonstrate that ·OH and $\cdot O_2^-$ are the dominant active species in the photodegradation reaction system. To further confirm the existence of active species ·OH and $\cdot O_2^-$ in the photodegradation process, the electron paramagnetic resonance (EPR) spectra of 70% CeO_2/g-C_3N_4 were tested (Fig. 7c and 7d). The obvious ESR signals are detected with DMPO−•OH and DMPO-•O_2^- adducts under the light irradiation, whereas the signals are not observed in the dark, signifying that both •OH and $\cdot O_2^-$ are generated during the photocatalytic degradation reactions. The results not only confirm that the built-in electronic field creating Z-scheme heterojunction is formed, but also show the superiority of ball milling obtained CeO_2/g-C_3N_4 for pollutant elimination.

4. Conclusions

In summary, effective Z-scheme heterojunction CeO_2/g-C_3N_4 photocatalysts were successfully prepared by a simple ball milling method, which display better adsorption and photodegradation efficiency for MB

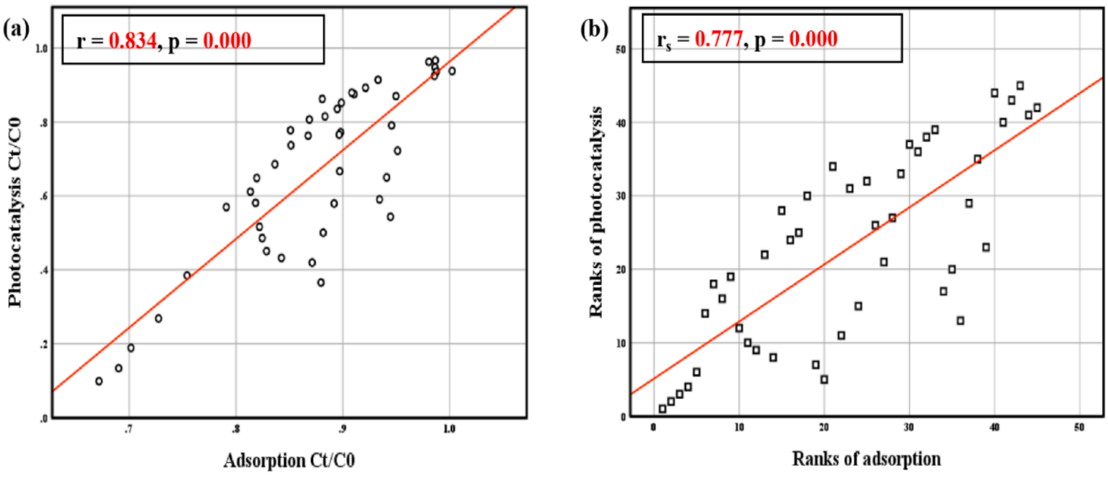

Fig. 6. (a) Pearson's and (b) Spearman's correlation between the adsorption and photodegradation rates of MB onto the samples.

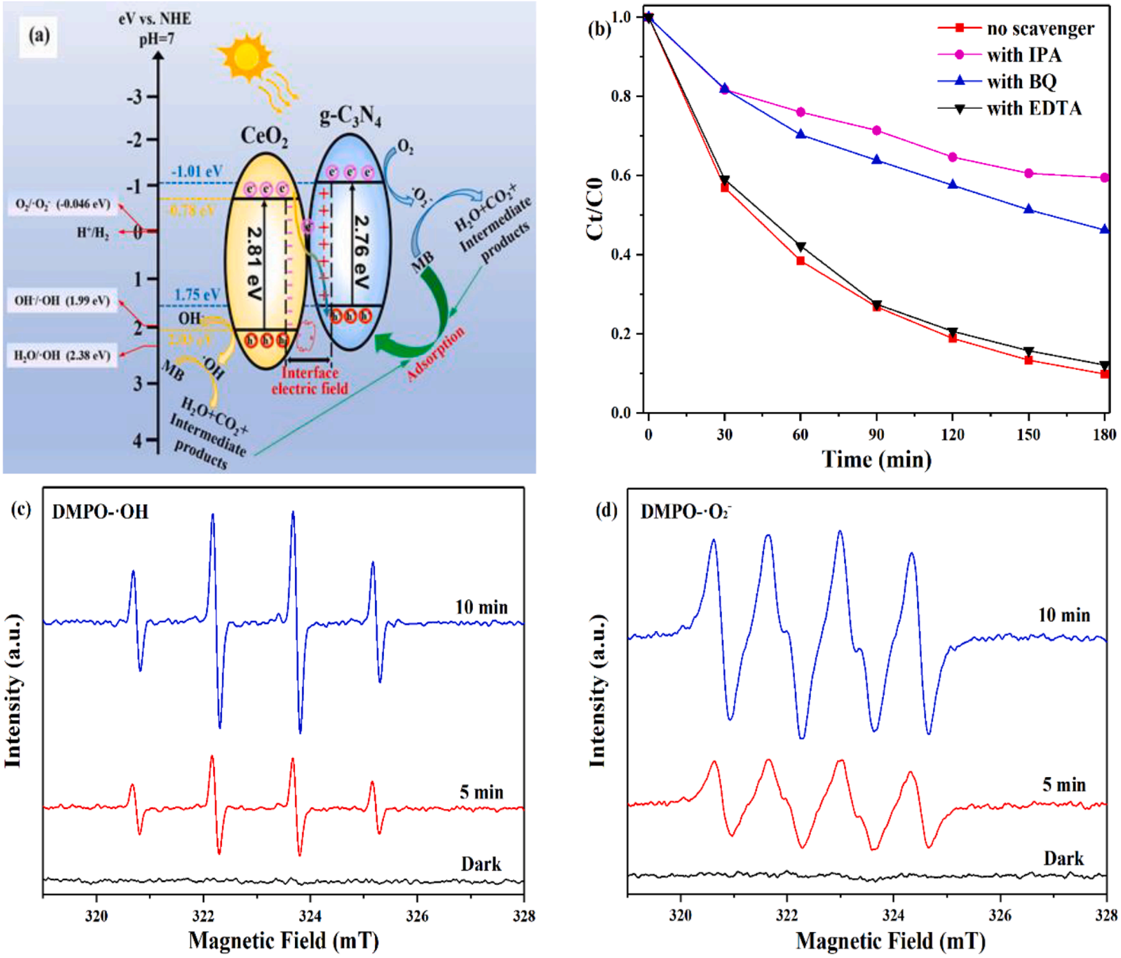

Fig. 7. (a) Schematic diagram of the mechanism of MB removal by CeO_2/g-C_3N_4 under UV light irradiation. (b) Effect of scavengers on photocatalytic activity of 70% CeO_2/g-C_3N_4. ESR spectra of 70% CeO_2/g-C_3N_4: (c) in aqueous dispersion for DMPO−•OH and (d) in methanol dispersion for DMPO-•O_2^- under light irradiation.

than individual CeO_2 or g-C_3N_4. The ball milling treatment strengthened the interfacial interaction, leading to increased light absorption, faster interfacial charge separation, stronger redox ability, more active oxygen radicals, and thereby thermodynamically enhanced photocatalytic performance. MB removal kinetics by the photocatalysts manifest the strong decontamination ability of heterojunction CeO_2/g-C_3N_4 due to the synergy between adsorption and photocatalytic degradation. These results indicate that adsorption ability and heterojunction construction are key factors controlling the removal efficiency of photodegradable pollutants, and ball milling can be used as an environmentally friendly and cost-effective method to synthesize heterojunction photocatalysts for environmental applications.

Declaration of Competing Interest

The authors declare that they have no known competing financial interests or personal relationships that could have appeared to influence the work reported in this paper.

Acknowledgment

W.Z., C.C. and L.D. would like to acknowledge the support of the National Natural Science Foundation of China (21707066, 21908092, 21677069, and 21773106).

Appendix A. Supplementary data

Supplementary data to this article can be found online at https://doi.org/10.1016/j.cej.2020.127719.

References

[1] M.B. Ahmed, J.L. Zhou, H.H. Ngo, W. Guo, Adsorptive removal of antibiotics from water and wastewater: Progress and challenges, Sci. Total Environ. 532 (2015) 112–126.

[2] M.M. Mian, G. Liu, Recent progress in biochar-supported photocatalysts: synthesis, role of biochar, and applications, RSC Adv. 8 (2018) 14237–14248.

[3] M. Shanmugam, A. Alsalme, A. Alghamdi, R. Jayavel, Enhanced Photocatalytic Performance of the Graphene-V_2O_5 Nanocomposite in the Degradation of Methylene Blue Dye under Direct Sunlight, ACS Appl. Mater. Interfaces 7 (2015) 14905–14911.

[4] W. Lei, T. Zhang, L. Gu, P. Liu, J.A. Rodriguez, G. Liu, M. Liu, Surface-Structure Sensitivity of CeO_2 Nanocrystals in Photocatalysis and Enhancing the Reactivity with Nanogold, ACS Catal. 5 (2015) 4385–4393.

[5] D.F. Li, K. Yang, X.Q. Wang, Y.L. Ma, G.F. Huang, W.Q. Huang, Enhancement of photocatalytic activity of combustion-synthesized CeO_2/C_3N_4 nanoparticles, Appl. Phys. A 120 (2015) 1205–1209.

[6] K. Kasinathan, J. Kennedy, M. Elayaperumal, M. Henini, M. Malik, Photodegradation of organic pollutants RhB dye using UV simulated sunlight on ceria based TiO_2 nanomaterials for antibacterial applications, Sci. Rep. 6 (2016) 38064–38075.

[7] X. Chen, L. Liu, Y. Feng, L. Wang, Z. Bian, H. Li, Z.L. Wang, Fluid eddy induced piezo-promoted photodegradation of organic dye pollutants in wastewater on ZnO nanorod arrays/3D Ni foam, Mater. Today 20 (2017) 501–506.

[8] W. Zou, B. Deng, X. Hu, Y. Zhou, Y. Pu, S. Yu, K. Ma, J. Sun, H. Wan, L. Dong, Crystal-plane-dependent metal oxide-support interaction in CeO_2/g-C_3N_4 for photocatalytic hydrogen evolution, Appl. Catal. B Environ. 238 (2018) 111–118.

[9] S. Petrović, L. Rožić, B. Grbić, N. Radić, P. Stefanov, S. Stojadinović, V. Jović, J. Lamovec, Effect of high energy ball milling on the physicochemical properties of

TiO_2–CeO_2 mixed oxide and its photocatalytic behavior in the oxidation reaction, React. Kinet., Mech. Catal. 127 (2019) 175–186.

[10] X.Y. Kong, W.Q. Lee, A.R. Mohamed, S.-P. Chai, Effective steering of charge flow through synergistic inducing oxygen vacancy defects and p-n heterojunctions in 2D/2D surface-engineered Bi_2WO_6/BiOI cascade: Towards superior photocatalytic CO_2 reduction activity, Chem. Eng. J. 372 (2019) 1183–1193.

[11] L. Zhu, H. Li, P. Xia, Z. Liu, D. Xiong, Hierarchical ZnO Decorated with CeO_2 Nanoparticles as the Direct Z-Scheme Heterojunction for Enhanced Photocatalytic Activity, ACS Appl. Mater. Interfaces 10 (2018) 39679–39687.

[12] J. Low, J. Yu, M. Jaroniec, S. Wageh, A.A. Al-Ghamdi, Heterojunction Photocatalysts, Adv. Mater. 29 (2017) 1601694–1601713.

[13] Y. Wang, H.B. Fang, Y.Z. Zheng, R. Ye, X. Tao, J.F. Chen, Controllable assembly of well-defined monodisperse Au nanoparticles on hierarchical ZnO microspheres for enhanced visible-light-driven photocatalytic and antibacterial activity, Nanoscale 7 (2015) 19118–19128.

[14] L. Zhu, H. Li, Z. Liu, P. Xia, Y. Xie, D. Xiong, Synthesis of the 0D/3D CuO/ZnO Heterojunction with Enhanced Photocatalytic Activity, J. Phys. Chem. C 122 (2018) 9531–9539.

[15] H.L. Wang, L.S. Zhang, Z.G. Chen, J.Q. Hu, S.J. Li, Z.H. Wang, J.S. Liu, X.C. Wang, Semiconductor heterojunction photocatalysts: design, construction, and photocatalytic performances, Chem. Soc. Rev. 43 (2014) 5234–5244.

[16] J. Yang, Y. Liang, K. Li, G. Yang, S. Yin, One-step low-temperature synthesis of 0D CeO_2 quantum dots/2D BiOX (X = Cl, Br) nanoplates heterojunctions for highly boosting photo-oxidation and reduction ability, Appl. Catal. B Environ. 250 (2019) 17–30.

[17] Y. Wang, X. Bai, F. Wang, S. Kang, C. Yin, X. Li, Nanocasting synthesis of chromium doped mesoporous CeO_2 with enhanced visible-light photocatalytic CO_2 reduction performance, J. Hazard. Mater. 372 (2019) 69–76.

[18] J. Tian, Y. Sang, Z. Zhao, W. Zhou, D. Wang, X. Kang, H. Liu, J. Wang, S. Chen, H. Cai, H. Huang, Enhanced photocatalytic performances of CeO_2/TiO_2 nanobelt heterostructures, Small 9 (2013) 3864–3872.

[19] M. Liang, T. Borjigin, Y. Zhang, B. Liu, H. Liu, H. Guo, Controlled assemble of hollow heterostructured g-C_3N_4@CeO_2 with rich oxygen vacancies for enhanced photocatalytic CO_2 reduction, Appl. Catal. B Environ. 243 (2019) 566–575.

[20] Q. Qiao, K. Yang, L.L. Ma, W.Q. Huang, B.-X. Zhou, A. Pan, W. Hu, X. Fan, G.-F. Huang, Facile in situ construction of mediator-free direct Z-scheme g-C_3N_4/CeO_2 heterojunctions with highly efficient photocatalytic activity, J. Phys. D: Appl. Phys. 51 (2018) 275302–275313.

[21] X. Liu, L. He, X. Chen, L. Du, X. Gu, S. Wang, M. Fu, F. Dong, H. Huang, Facile synthesis of CeO_2/g-C_3N_4 nanocomposites with significantly improved visible-light photocatalytic activity for hydrogen evolution, Int. J. Hydrogen Energy 44 (2019) 16154–16163.

[22] S. Tonda, S. Kumar, M. Bhardwaj, P. Yadav, S. Ogale, g-C_3N_4/NiAl-LDH 2D/2D Hybrid Heterojunction for High-Performance Photocatalytic Reduction of CO_2 into Renewable Fuels, ACS Appl. Mater. Interfaces 10 (2018) 2667–2678.

[23] M. Humayun, Z. Hu, A. Khan, W. Cheng, Y. Yuan, Z. Zheng, Q. Fu, W. Luo, Highly efficient degradation of 2,4-dichlorophenol over CeO_2/g-C_3N_4 composites under visible-light irradiation: Detailed reaction pathway and mechanism, J. Hazard. Mater. 364 (2019) 635–644.

[24] N. Tian, H. Huang, C. Liu, F. Dong, T. Zhang, X. Du, S. Yu, Y. Zhang, In situ co-pyrolysis fabrication of CeO_2/g-C_3N_4 n–n type heterojunction for synchronously promoting photo-induced oxidation and reduction properties, J. Mater. Chem. A 3 (2015) 17120–17129.

[25] R. Ma, S. Zhang, L. Li, P. Gu, T. Wen, A. Khan, S. Li, B. Li, S. Wang, X. Wang, Enhanced Visible-Light-Induced Photoactivity of Type-II CeO_2/g-C_3N_4 Nanosheet toward Organic Pollutants Degradation, ACS Sustainable Chem. Eng. 7 (2019) 9699–9708.

[26] T.V.M. Sreekanth, P.C. Nagajyothi, G.R. Dillip, Y.R. Lee, Determination of Band Alignment in the Synergistic Catalyst of Electronic Structure-Modified Graphitic Carbon Nitride-Integrated Ceria Quantum-Dot Heterojunctions for Rapid Degradation of Organic Pollutants, J. Phys. Chem. C 121 (2017) 25229–25242.

[27] S. Soren, I. Hota, A.K. Debnath, D.K. Aswal, K.S.K. Varadwaj, P. Parhi, Oxygen Reduction Reaction Activity of Microwave Mediated Solvothermal Synthesized CeO_2/g-C_3N_4 Nanocomposite, Front Chem. 7 (2019) 403–412.

[28] S.L. James, C.J. Adams, C. Bolm, D. Braga, P. Collier, T. Friscic, F. Grepioni, K. D. Harris, G. Hyett, W. Jones, A. Krebs, J. Mack, L. Maini, A.G. Orpen, I.P. Parkin, W.C. Shearouse, J.W. Steed, D.C. Waddell, Mechanochemistry: opportunities for new and cleaner synthesis, Chem. Soc. Rev. 41 (2012) 413–447.

[29] L. Cui, X. Ding, Y. Wang, H. Shi, L. Huang, Y. Zuo, S. Kang, Facile preparation of Z-scheme WO_3/g-C_3N_4 composite photocatalyst with enhanced photocatalytic performance under visible light, Appl. Surf. Sci. 391 (2017) 202–210.

[30] Y. Xin, G. Qiang, H. Xiaoyan, Y. Congxiang, A. Tao, W. Zhenjun, S. Guodong, S. Xinghua, Z. Peng, Fabrication of g-C_3N_4/MoS_2 Nanosheet Heterojunction by Facile Ball Milling Method and Its Visible Light Photocatalytic Performance, Rare Met. Mater. Eng. 47 (2018) 3015–3020.

[31] X. Zhou, N. Liu, J. Schmidt, A. Kahnt, A. Osvet, S. Romeis, E.M. Zolnhofer, V. R. Marthala, D.M. Guldi, W. Peukert, M. Hartmann, K. Meyer, P. Schmuki, Noble-Metal-Free Photocatalytic Hydrogen Evolution Activity: The Impact of Ball Milling Anatase Nanopowders with TiH_2, Adv. Mater. 29 (2017) 1604747–1604753.

[32] K. Zhu, Y. Lv, J. Liu, W. Wang, C. Wang, S. Li, P. Wang, M. Zhang, A. Meng, Z. Li, Facile fabrication of g-C_3N_4/SnO_2 composites and ball milling treatment for enhanced photocatalytic performance, J. Alloys Compd. 802 (2019) 13–18.

[33] X.L. Wang, W.Q. Fang, S. Yang, P. Liu, H. Zhao, H.G. Yang, Structure disorder of graphitic carbon nitride induced by liquid-assisted grinding for enhanced photocatalytic conversion, RSC Adv. 4 (2014) 10676–10679.

[34] Y. Guo, J. Li, Z. Gao, X. Zhu, Y. Liu, Z. Wei, W. Zhao, C. Sun, A simple and effective method for fabricating novel p–n heterojunction photocatalyst g-C_3N_4/$Bi_4Ti_3O_{12}$ and its photocatalytic performances, Appl. Catal. B Environ. 192 (2016) 57–71.

[35] X. Wei, X. Wang, B. Gao, W. Zou, L. Dong, Facile Ball-Milling Synthesis of CuO/Biochar Nanocomposites for Efficient Removal of Reactive Red 120, ACS Omega 5 (2020) 5748–5755.

[36] Y. Luo, X. Wei, B. Gao, W. Zou, Y. Zheng, Y. Yang, Y. Zhang, Q. Tong, L. Dong, Synergistic adsorption-photocatalysis processes of graphitic carbon nitrate (g-C_3N_4) for contaminant removal: Kinetics, models, and mechanisms, Chem. Eng. J. 375 (2019) 122019–122025.

[37] Y. Luo, B. Deng, Y. Pu, A. Liu, J. Wang, K. Ma, F. Gao, B. Gao, W. Zou, L. Dong, Interfacial coupling effects in g-C_3N_4/$SrTiO_3$ nanocomposites with enhanced H_2 evolution under visible light irradiation, Appl. Catal. B Environ. 247 (2019) 1–9.

[38] C. Chang, Y. Fu, M. Hu, C. Wang, G. Shan, L. Zhu, Photodegradation of bisphenol A by highly stable palladium-doped mesoporous graphite carbon nitride (Pd/mpg-C_3N_4) under simulated solar light irradiation, Appl. Catal. B Environ. 142–143 (2013) 553–560.

[39] D. Gao, Q. Xu, J. Zhang, Z. Yang, M. Si, Z. Yan, D. Xue, Defect-related ferromagnetism in ultrathin metal-free g-C_3N_4 nanosheets, Nanoscale 6 (2014) 2577–2581.

[40] M.-H. Wu, L. Li, Y.-C. Xue, G. Xu, L. Tang, N. Liu, W.-Y. Huang, Fabrication of ternary GO/g-C_3N_4/MoS_2 flower-like heterojunctions with enhanced photocatalytic activity for water remediation, Appl. Catal. B Environ. 228 (2018) 103–112.

[41] X. Yang, Z. Chen, J. Xu, H. Tang, K. Chen, Y. Jiang, Tuning the morphology of g-C_3N_4 for improvement of Z-scheme photocatalytic water oxidation, ACS Appl. Mater. Interfaces 7 (2015) 15285–15293.

[42] L. Liu, Y. Qi, J. Lu, S. Lin, W. An, Y. Liang, W. Cui, A stable Ag_3PO_4 @g-C_3N_4 hybrid core@shell composite with enhanced visible light photocatalytic degradation, Appl. Catal. B Environ. 183 (2016) 133–141.

[43] X. She, H. Xu, H. Wang, J. Xia, Y. Song, J. Yan, Y. Xu, Q. Zhang, D. Du, H. Li, Controllable synthesis of CeO_2/g-C_3N_4 composites and their applications in the environment, Dalton Trans. 44 (2015) 7021–7031.

[44] S.E. Pfenninger, The Dynamic Multicausality of Age of First Bilingual Language Exposure: Evidence From a Longitudinal Content and Language Integrated Learning Study With Dense Time Serial Measurements, The Modern Language Journal 104 (2020) 662–686.

[45] S. Hu, L. Ma, J. You, F. Li, Z. Fan, G. Lu, D. Liu, J. Gui, Enhanced visible light photocatalytic performance of g-C_3N_4 photocatalysts co-doped with iron and phosphorus, Appl. Surf. Sci. 311 (2014) 164–171.

[46] W. Zou, Y. Shao, Y. Pu, Y. Luo, J. Sun, K. Ma, C. Tang, F. Gao, L. Dong, Enhanced visible light photocatalytic hydrogen evolution via cubic CeO_2 hybridized g-C_3N_4 composite, Appl. Catal. B Environ. 218 (2017) 51–59.

[47] T. Chen, J. Zhang, H.L. Ge, M.X. Li, Y. Li, B. Liu, T. Duan, R. He, W.K. Zhu, Efficient extraction of uranium in organics-containing wastewater over g-C_3N_4/GO hybrid nanosheets with type-II band structure, J. Hazard. Mater. 384 (2020) 121383–121390.

[48] J. Lei, H.H. Liu, D.R. Yin, L.H. Zhou, J.A. Liu, Q. Chen, X.D. Cui, R. He, T. Duan, W. K. Zhu, Boosting the Loading of Metal Single Atoms via a Bioconcentration Strategy, Small 16 (2020), e1905920.

[49] M. Jourshabani, Z. Shariatinia, A. Badiei, Facile one-pot synthesis of cerium oxide/sulfur-doped graphitic carbon nitride (g-C_3N_4) as efficient nanophotocatalysts under visible light irradiation, J. Colloid Interface Sci. 507 (2017) 59–73.

[50] Q. Cai, J. Shen, Y. Feng, Q. Shen, H. Yang, Template-free preparation and characterization of nanoporous g-C_3N_4 with enhanced visible photocatalytic activity, J. Alloys Compd. 628 (2015) 372–378.

[51] T. Paul, D. Das, B.K. Das, S. Sarkar, S. Maiti, K.K. Chattopadhyay, $CsPbBrCl_2$/g-C_3N_4 type II heterojunction as efficient visible range photocatalyst, J. Hazard. Mater. 380 (2019) 120855–120867.

[52] F. Zeng, W.Q. Huang, J.H. Xiao, Y.Y. Li, W. Peng, W. Hu, K. Li, G.F. Huang, Isotype heterojunction g-C_3N_4/g-C_3N_4 nanosheets as 2D support to highly dispersed 0D metal oxide nanoparticles: Generalized self-assembly and its high photocatalytic activity, J. Phys. D: Appl. Phys. 52 (2019) 025501–025511.

[53] T. Chen, B. Liu, M.X. Li, L. Zhou, D.J. Lin, X.B. Ding, J. Lian, J.W. Li, R. He, T. Duan, W.K. Zhu, Efficient uranium reduction of bacterial cellulose-MoS_2 heterojunction via the synergistically effect of Schottky junction and S-vacancies engineering, Chem. Eng. J. 406 (2021) 126791–126799.

[54] W. Liu, J. Zhou, Z. Hu, Nano-sized g-C_3N_4 thin layer @ CeO_2 sphere core-shell photocatalyst combined with H_2O_2 to degrade doxycycline in water under visible light irradiation, Sep. Purif. Technol. 227 (2019) 115665–115674.

[55] X.J. Wen, C.G. Niu, L. Zhang, C. Liang, G.M. Zeng, A novel Ag_2O/CeO_2 heterojunction photocatalysts for photocatalytic degradation of enrofloxacin: possible degradation pathways, mineralization activity and an in depth mechanism insight, Appl. Catal. B Environ. 221 (2018) 701–714.

[56] W. Zou, B. Gao, Y.S. Ok, L. Dong, Integrated adsorption and photocatalytic degradation of volatile organic compounds (VOCs) using carbon-based nanocomposites: A critical review, Chemosphere 218 (2019) 845–859.

[57] T. Chen, J. Zhang, M.X. Li, H.L. Ge, Y. Li, T. Duan, W.K. Zhu, Biomass-derived composite aerogels with novel structure for removal/recovery of uranium from simulated radioactive wastewater, Nanotechnol. 30 (2019) 455602–455611.

[58] T. Chen, P.H. Shi, J. Zhang, Y. Li, T. Duan, L.C. Dai, L. Wang, X.F. Yu, W.K. Zhu, Natural polymer konjac glucomannan mediated assembly of graphene oxide as versatile sponges for water pollution control, Carbohydr. Polym. 202 (2018) 425–433.

[59] J. Hauke, T. Kossowski, Comparison of Values of Pearson's and Spearman's Correlation Coefficients on the Same Sets of Data, Quaestiones Geographicae 30 (2011) 87–93.

[60] H.L. Zhang, W. Liu, A. Li, D. Zhang, X.Y. Li, F.W. Zhai, L.H. Chen, L. Chen, Y. L. Wang, S. Wang, Three Mechanisms in One Material: Uranium Capture by a Polyoxometalate-Organic Framework through Combined Complexation, Chemical Reduction, and Photocatalytic Reduction, Angew. Chem., Int. Ed. Engl. 58 (2019) 16110–16114.

[61] H. Li, F.W. Zhai, D.X. Gui, X.X. Wang, C.F. Wu, D. Zhang, X. Dai, H. Deng, X.T. Su, J. Diwu, Z. Lin, Z.F. Chai, S. Wang, Powerful uranium extraction strategy with combined ligand complexation and photocatalytic reduction by postsynthetically modified photoactive metal-organic frameworks, Appl. Catal. B Environ. 254 (2019) 47–54.

[62] F. Galindo, R. Gómez, M. Aguilar, Photodegradation of the herbicide 2,4-dichlorophenoxyacetic acid on nanocrystalline TiO_2–CeO_2 sol–gel catalysts, J. Mol. Catal. A: Chem. 281 (2008) 119–125.